Super-diffusion affected by hydrofacies mean length and source geometry in alluvial settings

Maosheng Yin[1]

Yong Zhang[2*]

Rui Ma[1*]

Geoffrey Tick[2]

Marco Bianchi[3]

Chunmiao Zheng[4]

Wei Wei[5]

Song Wei[4]

Xiaoting Liu[6]

1. School of Environmental Studies, China University of Geosciences, Wuhan, Hubei 430074, China
2. Department of Geosciences, University of Alabama, Tuscaloosa, AL 35487, USA
3. British Geological Survey, Environmental Science Centre, Nottingham, UK
4. School of Environmental Science & Engineering, Southern University of Science and Technology, Shenzhen 518055, Guangzhou, China
5. Guangdong Provincial Key Laboratory of Soil and Groundwater Pollution Control & Jiangsu Provincial Key Laboratory of Materials Cycling and Pollution Control, Jiangsu Engineering Laboratory of Water and Soil Eco-remediation, School of Environment, Nanjing Normal University, Nanjing 210023, China
6. College of Mechanics and Materials, Hohai University, Nanjing, Jiangsu 210098, China

*Corresponding authors: Yong Zhang at yzhang264@ua.edu and Rui Ma at rma@cug.edu.cn

For submission to ***Journal of Hydrology***

Abstract: Dissolved-phase contaminants experiencing enhanced diffusion (i.e., "super-diffusion") with a pronounced leading plume edge can pose risk for groundwater quality. The drivers for complex super-diffusion in geological media, however, are not fully understood. This study investigates the impacts of hydrofacies' mean lengths and the initial source geometry, motivated by a hydrofacies model built recently for the well-known MADE aquifer, on the spatial pattern of super-diffusion for two-dimensional alluvial aquifer systems. Monte Carlo simulations show that the bimodal velocity distribution, whose pattern is affected by the hydrofacies' mean lengths, leads to super-diffusion of solutes with a bi-peak plume snapshot in alluvial settings where advection dominates transport. A larger longitudinal mean length (i.e., width) for hydrofacies with high hydraulic conductivity (*K*) enhances the connectivity of preferential pathways, resulting in higher values in the bimodal velocity distribution and an enhanced leading front for the bi-peak plume snapshot, while the opposite impact is identified for the hydrofacies' vertical mean length (i.e., thickness) on the bi-peak super-diffusion. A multi-domain non-local transport model is then proposed, extending upon the concept of the distributed-order fractional derivative, to quantify the evolution of bi-peak super-diffusion due to differential advection and mobile-mobile mass exchange for solute particles moving in hydrofacies with distinct *K*. Results show that the bi-peak super-diffusion identified for the MADE site and perhaps the other similar aquifers, which is affected by the initial source geometry at an early stage and the thickness and width of high-*K* hydrofacies during all stages, can be quantified by the mobile-mobile fractional-derivative model. Scale dependency, porous medium dimensionality, and stochastic model comparison are also discussed to further explore the nature of bi-peak super-diffusion in alluvial systems.

Keywords: Super-diffusion; Alluvial aquifer; Hydrofacies model; Monte Carlo simulation

1. Introduction

Super-diffusive transport (defined by the faster than linear growth of a solute plume's second central moment (or variance) in time) in heterogeneous aquifers, which is usually characterized by an apparent leading edge of the solute plume, can pose a high risk to groundwater quality (Benson et al., 2001; Schumer et al., 2003a; Zhang et al., 2009). Super-diffusion differs significantly from sub-diffusion (defined by the slower than linear growth of the plume variance in time) which is mainly characterized by solute retention and whose transport behavior can be characterized by various stochastic models (Haggerty and Gorelick, 1995; Schumer et al., 2003b; Berkowitz et al., 2006; Zhang et al., 2010; Dentz et al., 2015; Tyukhova et al., 2016; among many others). Super-diffusion has mainly been identified for a few field tracer tests, including those conducted at the well-known MAcroDispersion Experiment (MADE) site (a heterogeneous alluvial depositional aquifer system) focused by hydrogeological modelers for over three decades (Adams and Gelhar, 1992; Zheng et al., 2011). Dynamics of super-diffusion in real-world aquifer systems, including the MADE site, have not been fully developed or well understood, motivating this study.

Efforts have been made to identify the mechanisms controlling super-diffusion in groundwater for decades. Numerical and analytical analyses were carried out first, revealing that the extensive "heavy" tailing behavior (especially the power-law distributed) and long-range correlation of hydraulic conductivity (K) can lead to early arrivals of solutes in heterogeneous porous media (Sahimi, 1993; Benson et al., 2001; Herrick et al., 2002; Saadatfar and Sahimi, 2002;

Kohlbecker et al., 2006; Dentz and Bolster, 2010). Spatial moments analysis also showed that super-diffusive transport via random walk motion can be driven by power-law distributed, correlated velocities (Dentz and Bolster, 2010) or as a result of layered media with specific velocity distributions (Bouchaud et al., 1990). Salamon et al. (2007) conducted numerical experiments and also found that the strong variation and continuity of K in space caused the heavy (extended) leading edge of the tracer plumes observed at the MADE site. Most of these studies revealed the physical condition for super-diffusion, i.e., a random K field with a large variance (and long correlation lengths for most cases). Particularly, the wide contrasts in hydraulic properties of the sediments forming typical alluvial systems can promote super-diffusion, because the interconnected, high-K deposits (such as ancient channels) surrounded by relatively low-K deposits, representing the common internal architecture of an alluvial setting, can guarantee the highly correlated K with a large variance (Fogg and Zhang, 2016).

This typical alluvial structure can be reliably captured by the transition probability based geostatistical tool called "T-PROGS" (Carle and Fogg, 1996, 1997; Carle, 1999), which provides a feasible way to systematically explore anomalous transport in alluvial systems. T-PROGS can capture major properties of hydrofacies, including their global volumetric proportion, mean lengths (i.e., thickness/width along the vertical/longitudinal direction), and juxtaposition tendency, motivating the numerical exploration of anomalous transport for models of hydrofacies or lithofacies (representing the assemblage of deposits with similar hydrological properties).

Hydrofacies models built by T-PROGS in Zhang et al. (2013) and Bianchi and Zheng (2016), however, led to contrasting conclusions describing the generation of super-diffusion. Zhang et al. (2013) found that although the hydrofacies models do capture the strong spatial variation and continuity of K, they cannot generate super-diffusion with a heavy leading plume front, although apparent sub-diffusion with extensive late-time concentration tailing behavior dominates the solute breakthrough curves (BTCs). Contrarily, the recent work by Bianchi and Zheng (2016) successfully captured super-diffusion with an obvious and pronounced leading edge in the plume snapshots observed at the MADE site (at the sample cycles after ~132 days), using the T-PROGS-generated hydrofacies model. A percolated hydrofacies with a significantly high K (two orders of magnitude higher than the other hydrofacies) was found to cause the rapid movement of the leading plume edge (Bianchi and Zheng, 2016). In T-PROGS, the hydrofacies' mean lengths significantly affect the hydrofacies' connectivity, while the estimation of the hydrofacies' mean lengths (especially the horizontal mean length) contains high uncertainty due to the typically limited number of boreholes. The impacts of hydrofacies' mean lengths along different directions on super-diffusion were not systematically addressed in Bianchi and Zheng (2016), except for a preliminary sensitivity test. To reliably identify the major geological mechanisms controlling super-diffusion in typical alluvial systems, discrepancy between these two studies needs be explored by systematically extending the hydrofacies model for addressing the facies' mean length uncertainty on solute transport. Therefore, the exploration of such mechanisms is the major focus of this study.

The following content of this work is organized as follows. **Section 2** introduces the Monte Carlo simulations with multiple scenarios of hydrofacies models generated by T-PROGS to explore anomalous transport in the alluvial settings. **Section 3** presents the numerical results for the scenarios, by focusing on the behavior and mechanism of super-diffusion with a bi-peak plume snapshot. **Section 4** discusses the hydrogeological mechanisms dominating bi-peak super-diffusion by analyzing the velocity distribution, the impact of major properties of hydrofacies on super-diffusion, and the pattern of plume snapshots changing with the initial source geometry. A novel mobile-mobile transport model is then proposed to quantify and interpret the bimodal distribution of the pollutant snapshots. **Section 5** presents the main conclusions of the study. The super-diffusion with bi-peak snapshots and its hydrogeological interpretation, as well as its stochastic quantification, are the new contributions of this work and improve our understating in the nature of anomalous transport through complex aquifers on the scale of a few hundred meters.

2. Method of Monte Carlo simulations from hydrofacies model to pollutant transport

To explore the dynamics of tracers transport in alluvial settings with intrinsic heterogeneity, a numerical approach with three main steps was used by adopting the procedures in Zhang et al. (2013) and Bianchi & Zheng (2016). First, T-PROGS was used to generate two-dimensional (2-*d*), different alluvial settings with various hydrofacies structures (Carle and Fogg, 1997). Monte Carlo simulations of the hydrofacies distribution lead to the random K fields. Second, steady-state groundwater flow fields were calculated using a block-centered finite difference model (Harbaugh, 2006). Third, conservative tracer transport was simulated using the MT3D program (Zheng et al., 2010). The following subsections briefly describe these steps.

2.1 Modeling hydrofacies structures and hydraulic conductivity fields

T-PROGS (Carle, 1999; Carle and Fogg, 1997) was used to generate hydrofacies structures that can be representative of different alluvial aquifers. To construct numerical models representing major properties of real-world aquifers, the geostatistical characters/properties of the MADE aquifer identified by Bianchi and Zheng (2016) is used as a reference. As in the previous work, the generated aquifers are therefore characterized by five hydrofacies, including (1) a highly conductive gravel (HCG), (2) gravel with sand (GS), (3) sand gravel and fines (SGF), (4) sand and gravel (SG), and (5) well-sorted sand (S). The hydrofacies properties, including the hydraulic conductivity, mean lengths, and the volumetric proportion listed in **Table 1** are also consistent with the lithological model proposed by Bianchi and Zheng (2016).

A 2-*d* vertical profile of the aquifer with a dimension of 300 m in length and 40 m in thickness is used, with the grid size of 10 m and 0.5 m along the longitudinal and vertical directions, respectively. The same model and gird dimensions are used for the following flow and transport models. The sensitivity of transport dynamics to the grid size is discussed in the supplementary material (section S4), to evaluate the feasibility of the grid resolution selected in this study.

There are three modifications of the hydrofacies modeling in Bianchi and Zheng (2016). *First*, multiple scenarios containing different mean lengths along the vertical direction (i.e., thicknesses) or the longitudinal direction (i.e., widths) for hydrofacies are developed to account for the uncertainty of hydrofacies mean lengths and their potential impact on transport. *Second*, no hard-conditional data are used in most scenarios when running T-PROGS, so that the resultant hydrofacies models can capture the maximum spatial variation of hydrofacies necessary for a systematic analysis. *Third*, the 3-*d* models used by Bianchi and Zheng (2016) are simplified to 2-*d* models, since the 2-*d* models provide the simplest framework to control the longitudinal and vertical correlations of K and evaluate the impact of K structures on solute transport. The impact of model dimension on super-diffusion will be discussed in the supplementary material (section S2).

Eight scenarios are designed, with 100 realizations for each scenario, to investigate the influence of the internal aquifer structure on super-diffusion. Scenario 1 is the basic case representing the general statistics obtained from the MADE aquifer, with parameters estimated by Bianchi and Zheng (2016) (**Table 1**). Scenarios 2, 3, and 4 have the thickness (i.e., the vertical mean length) of 1.5, 2.0, and 2.5 times larger than that of the base scenario for all the hydrofacies, respectively. Scenarios 5, 6, and 7 have a longitudinal mean length or width for each hydrofacies 1.25, 1.5, and 2.0 times larger than the base case, respectively.

Scenario 8 is designed to investigate the influence of the contaminant source vertical extension on solute transport. Four vertical line sources with the length increasing from 2, 5, 20, to 40 m (i.e., 1/20, 1/4, 1/2 and 1.0 time of the aquifer thickness, respectively) are considered in this study. To decrease the impact of low-K zones on the injection of the initial pollutant source, an aggregate of high-K HCG facies located at z=20~22 m and x=5 m is used as the hard conditional data (configuration) when building the realizations for Scenario 8, and this zone is selected as the midpoint of the line source. The same strategy was used by Zhang et al. (2013) in a similar Monte

Carlo study. **Fig. 1** shows one realization arbitrarily selected (realization #1) for each scenario.

2.2 Modeling of groundwater flow and solute transport

The steady-state flow fields are calculated using MODFLOW (Harbaugh, 2006), with the specified head boundary condition defined for the two vertical boundaries (left and right boundaries) and the no-flow boundary condition for the two horizontal boundaries (top and bottom boundaries). A ratio between the vertical and longitudinal K, 0.13, based on the pumping test conducted at the MADE site (Bianchi and Zheng, 2016; Boggs et al., 1990), is used in the groundwater flow modeling. The general hydraulic gradient of 0.006 is used in this study, which is similar to the one (0.0058) used by Guan et al. (2008). The average K (**Table 1**) is assigned for each hydrofacies when calculating groundwater flow.

The finite difference transport code MT3DMS (Zheng et al., 2010) is then used to calculate solute transport. A vertical instantaneous line source with the uniform concentration is used in Scenarios 1 to 7. In Scenario 8, various lengths (2, 5, 20, and 40 m) of the vertical line source is considered to investigate the impact of the initial source scale on solute transport. The initial source for all scenarios is located at $x = 5$ m. The downgradient boundary along the longitudinal direction is defined as the zero-value Neumann boundary (i.e., the free exit boundary), while the top and bottom boundaries are no-flux boundaries. The molecular diffusion coefficient is 1.16×10^{-9} m^2/s, representing the diffusivity for tritium in water (Bianchi and Zheng, 2016). The effective porosity for each hydrofacies is listed in **Table 1**. The longitudinal dispersivity α_L is 1 m (which is 1/10 of the grid dimension), and the vertical dispersivity α_V is two orders of magnitude lower than α_L (Llopis-Albert and Capilla, 2009; Bianchi and Zheng, 2016). The sensitivity of super-diffusion on dispersivity will be addressed in the supplementary material (section S4).

3. Results

The ensemble average of the simulated plume snapshots for all the 100 realizations for each scenario is calculated and shown below (**Fig. 2~5**). The 1-*d* normalized longitudinal mass distribution at 27, 132, 224 and 328 days (after the release of the contaminant source), which present the four sample snapshots during the MADE-2 experiment (Bogg et al.,1990), is also plotted for further analysis. The variance of solute plumes is also calculated (shown by **Fig. S4**), providing clear evidence for super-diffusion of the simulated transport. The following subsections introduce the plume snapshots for each scenario in order to explore the impact of medium architecture and the initial concentration distribution on solute transport in alluvial systems.

3.1 Impact of hydrofacies' vertical mean length (i.e., thickness) on super-diffusion

The calculated mass distribution for scenarios 1~4 with different thicknesses for hydrofacies is depicted in **Fig. 2**. Super-diffusive transport is characterized by the plume's apparent leading front moving quickly along preferential pathways, while a large portion of solute remains near the initial source location.

The transport simulations also show that a smaller thickness of hydrofacies leads to a better connectivity of the high-*K* zones, which can enhance the downstream expansion of the plume front.

In addition, the different shape (i.e., skewness) of the simulated plume snapshots (**Fig. 2**) imply that the hydrofacies' thickness also affects the mass ratio of contaminants in the relatively high and low velocity zones. Particularly, the scenario with thicker hydrofacies (such as scenario 4) tends to delay (retain) more contaminants near the source and release less mass downgradient.

Therefore, the hydrofacies' thickness has the opposite impact on the two edges of the plume snapshot. A thicker hydrofacies, in fact, enhances the trailing edge due to the longer path for slow advection, while a thinner hydrofacies promotes the longitudinal facies/flow connection and hence enhances the downgradient migration of the plume's leading edge.

3.2 Impact of hydrofacies' longitudinal mean length (i.e., width) on super-diffusion

Fig. 3 depicts the simulated evolution of contaminant snapshots for scenarios 1, 5, 6, and 7, with different widths for hydrofacies. Results show that a larger width for the hydrofacies causes faster transport of the plume's leading edge, which is opposite to the effect of hydrofacies' thickness on super-diffusion. A similar result was found by Bianchi and Pedretti (2017), who showed that a larger horizontal mean length led to a more slant distribution for solute particles' arrival times. In addition, the hydrofacies' width only slightly affects the plume's trailing edge, which is different from the result shown in **section 3.1** whereby the hydrofacies' thickness can affect both edges of the plume snapshot.

3.3 Impact of the size of the initial contaminant source on super-diffusion

Fig. 4 shows the simulated plume snapshots for scenarios 8 with different sizes for the initial source. The initial source condition can significantly impact super-diffusion by affecting the overall pattern of plume snapshots. Strong super-diffusion is identified for all of the initial source-lengths evaluated in this study. On one hand, a larger initial source (in which orientation is perpendicular to the general flow direction) causes more solute particles to remain in the low velocity zones around the initial source, resulting in a more (positively) skewed plume snapshot. On the other hand, when the source size is much smaller (i.e., ≤2 m) and can be approximated as a point source (all mass located in the high-K zone initially), solute particles can move fast and form a distinct plume peak.

3.4 Two-dimensional plume snapshot

To directly view the solute transport process in heterogeneous structures, the spatial distribution of K and the corresponding 2-d snapshot of the plume front at different times for one realization in scenario 1 are plotted in **Fig. 5a** and **Fig. 5b**, respectively. The results show that the preferential flow path generated by continuous high-K hydrofacies has a great impact on plume evolution and is the main reason for super-diffusion. Meanwhile, a larger fraction of solute located at the relatively less permeable zone moves slowly. Another interesting phenomenon shown in **Fig. 5b** is that while the preferential path generates super-diffusion, a front peak can also arise when a fraction of solutes moves faster along the preferential path. This bi-peak solute transport in alluvial aquifers will be further discussed and modeled in **section 4**.

4. Discussion

Super-diffusion for conservative tracers observed in the Monte Carlo simulations is mainly driven by the internal structure of the alluvial aquifer settings, where the detailed mechanism is discussed below. Particularly, we analyze the relationship among the medium's architecture, the velocity distribution, and anomalous transport characteristics. A novel physical model is then proposed to quantify the observed anomalous transport in the alluvial aquifers. The applicability of another popular stochastic model (the time nonlocal transport model) is discussed in the supplementary material to further explore the nature of bi-peak super-diffusion in alluvial systems.

4.1 Statistics of the Eulerian velocity

To calculate the velocity distribution for each scenario, we adopted the approach proposed by Hyman et al. (2019). Particularly, we define the magnitude of the Eulerian velocity using $v_e(x,z) = \|u(x,z)\|$, where $u(x,z)$ is the velocity simulated by our flow model. The PDF of the Eulerian velocity v in the flow domain Ω_e, denoted as $p_e(v)$, is given as:

$$p_e(v) = \frac{1}{U_e}\sum_{\Omega_e} \delta[v - v_e(x,z)]dU, \qquad (1)$$

where U_e is the domain's volume, δ is the Dirac delta function, dU is the volume of the cell in the groundwater flow model, and x and z are the longitudinal and vertical coordinates, respectively.

Since we consider an instantaneous line source in a rectangular aquifer under the condition of no-flow bottom/top boundaries, the longitudinal velocity is the main factor that may control the solute plume's longitudinal mass distribution. Therefore, to reveal the dominant mechanism of solute transport in alluvial structures, the longitudinal velocity is analyzed in detail herein. For each scenario, velocities of ~24,000 grids are counted, resulting in a solid PDF. **Fig. 6** shows that there are two peaks in the calculated velocity distribution with a broad spectrum ranging mostly between 1.0×10^{-4} m/d and 1.0×10^{1} m/d. To provide a more quantitative view, several key statistics of the velocity distribution are listed in **Table 2**. Notably, the percentage of the slow velocity zone (represented by "$P(v \leq v_m)$" in **Table 2**) is close to the total volumetric proportion (~0.88) of the hydrofacies excluding the high-K HCG, and the two velocity zones may be separated by the poor connectivity of some HCGs. A larger width for hydrofacies results in a slightly smaller fraction of the low velocity zone (**Table 2**), since the model with a larger width for hydrofacies can produce better longitudinal connectivity for high-K hydrofacies which in turn increases the proportion of high velocities in the velocity PDF. The opposite impact can be found for the hydrofacies thickness: thicker hydrofacies slightly increase the fraction of the low velocity zone (**Table 2**), likely due to the decreased longitudinal connectivity.

The bimodal distribution of velocity (**Fig. 6**) sheds light on the formation of super-diffusion and may explain the plume snapshots generated for different hydrofacies scenarios. The second peak of the velocity PDF, representing the high velocity, is associated with preferential flow paths for solute particles that exhibit the super-diffusion behavior. The proportion of the high to low velocity zones is approximately 10% to 90%, respectively (**Table 2**), indicating that most of the solute particles are transporting in the low velocity zone while the remaining particles move fast in the high velocity zone, generating the positively skewed plume snapshot and the overall super-diffusive transport behavior.

The vertical and longitudinal mean lengths of hydrofacies have significant and varied influences on the distribution of the longitudinal velocity. On one hand, as shown in **Fig. 6**, the hydrofacies' thickness affects the distribution of both the low and high velocities of moving solutes. Thicker hydrofacies lead to a higher percentage of the low velocity zones and shorter distances between the two peaks of the velocity PDF. On the other hand, the hydrofacies' width mainly affects the distribution of the high velocities with little associated impact on the low velocities (**Fig. 6**). Wider hydrofacies produce higher velocities and therefore separate the two contrasting velocity zones further in the velocity PDF. These results are consistent with the Monte Carlo simulations shown in **section 3** and provide further insight on the interpretation of the impact of alluvial setting's architecture on solute transport.

4.2 Correlation between hydraulic conductivity and velocity field

The relationship between the velocity field and the hydraulic conductivity field had been explored by various studies. For example, Veneziano and Tabaei (2004) and Veneziano and Essiam (2004) found a clear relationship between the velocity field and statistics of the K field. Herrick et al. (2002) and Kohlbecker et al. (2006) investigated the relationship between the heavy-tailed logarithm K and the heavy tailed log velocity distribution, and an empirical equation was proposed by Kohlbecker et al. (2006) to predict the tail of the velocity PDF based on the K distribution. A recent work in revealing the relationship between K and v (Bianchi and Pedretti, 2017) used a novel metric, *geological entropy*, and established a quantitative relationship between structure settings and the velocity distribution. The geological entropy was found to be a promising way to describe heterogeneous structure and predict solute transport (Bianchi and Pedretti, 2018).

In this section, we investigate the origin of the bimodal velocity distribution and focus on the influence of medium architecture on the relationship between the distributions of K and v. The frequency of the random K distribution (**Fig. S5**) clearly shows a bimodal pattern with the majority of K near $1\times10^{0.5}$ m/d and a smaller peak but a much larger K around $1\times10^{2.5}$ m/d. The similar bimodal characteristics of the random K field and the velocity's spatial distribution imply a direct correlation between these two random fields.

The spatial distributions of K and v of one realization for scenario 1 are shown in **Fig. 7**, illustrating a positive correlation between the spatial distribution of high K and large velocities. We calculate the coefficient of the spatial correlation between K and v using

$$C_r(K', v') = \frac{Cov(K', v')}{\sqrt{Var(K')\ Var(v')}} \quad , \tag{2}$$

where K' and v' are the spatial distributions of the normalized $\log_{10}(K)$ and the longitudinal velocity, respectively. The calculated correlation coefficient C_r between K and v is shown in **Fig. 8** for the scenarios with different mean lengths of hydrofacies. The porous medium's architecture setting has a significant impact on the correlation between K and v distributions. For example, when the width for hydrofacies is doubled, C_r increases from 0.737 to 0.784. This positive impact may be due to the better connectivity of K with wider hydrofacies. Contrarily, when the hydrofacies' thickness increases by 2.5 times, C_r decreases from 0.737 to 0.691. This negative impact may be due to the fact that thicker hydrofacies result in more high-*K* zones surrounded by the low-*K* zones, resulting in an overall lower proportion of high velocity zones (or isolation of high *K* zones) for solute transport.

4.3 Quantify bimodal super-diffusion using a distributed-order fractional-derivative model

To capture super-diffusion with multiple peaks in the plume snapshot, we adopt the concept of the distributed-order fractional derivative (Lorenzo and Hartley, 2002; Chechkin et al., 2002):

$$\int_1^m a(r)\,\mathfrak{D}_+^r u(x)dr = f(x) \ , \tag{3}$$

where the variable r ($1<r\leq 2$) denotes the order of the space fractional derivative, $a(r)$ is the weight for order r, and the symbol $\mathfrak{D}_+^r$ denotes the positive Riemann-Liouville fractional derivative (Miller and Ross, 1993):

$$\mathfrak{D}_+^r u(x) = \frac{\partial^r}{\partial x^r}u(x) = \frac{1}{\Gamma(2-r)}\frac{\partial^2}{\partial x^2}\int_{-\infty}^{x} u(y)(x-y)^{1-r}\ dy \ , \tag{4}$$

where $\Gamma(\cdot)$ represents the Gamma function. The multi-term (i.e., discrete components) version of the distributed-order fractional derivative equation takes the form (Diethelm and Ford, 2009):

$$\sum_{i=1}^{k} a_i\,\mathfrak{D}_*^{r_i} u(x) = f(x) \ , \tag{5}$$

which can be used to quantify the impact of multiple mobile zones (each with a distinct memory kernel or index) on the material dynamics. The distributed-order time fractional-derivative models, which replace the space fractional derivative in the above formula using the time fractional derivative, have been applied to decelerating solute sub-diffusion and the other random processes with multiple scaling (Mainardi et al. 2008; Eab and Lim, 2011; Gorenflo et al., 2015). To the best of our knowledge, the distributed-order space fractional-derivative model has not been applied for real-world or synthetic groundwater solute transport problems.

The multi-term distributed-order fractional derivative equation leads logically to the 1-*d*, Multi-Domain, tempered space Fractional-Derivative Model (MD-tsFDM) proposed by this study. The total mass M_t of the MD-tsFDM within a representative elementary volume (REV) is calculated by

$$M_t(x,t) = \sum_{i=1}^{N} C_i(x,t)\ \theta_i \varphi_i U_{REV} \quad , \tag{6}$$

where $C_i(x,t)$ $[M/L^3]$ is the concentration within the *i-th* domain at location x and time *t*, θ_i [-] and φ_i [-] are the average porosity and the proportion of the *i*-th domain, N [-] is the total number of domains, and U_{REV} $[L^3]$ is the volume of the REV. To capture the strong super-diffusive transport observed in the Monte Carlo simulations discussed above, the space fractional-derivative equation with a truncation parameter proposed by Baeumer and Meerschaert (2010) is selected:

$$\partial_t C_1(x,t) = -v_1 \partial_x C_1(x,t) + D_1 \partial_x^{\alpha_1,\lambda_1} C_1(x,t) - W_1(x,t) \tag{7a}$$

$$\partial_t C_2(x,t) = -v_2 \partial_x C_2(x,t) + D_2 \partial_x^{\alpha_2,\lambda_2} C_2(x,t) + W_2(x,t) \tag{7b}$$

where $W(\mathrm{x},\mathrm{t})$ is the mass exchange between the two mobile domains:

$$W_i(x,t) = \frac{\omega}{\varepsilon_i \varphi_i}[C_1(x,t) - C_2(x,t)] \tag{8}$$

and the operator $\partial_x^{\alpha,\lambda}$ in (7) denotes the tempered fractional derivative and can be calculated by (Baeumer and Meerschaert, 2010):

$$\partial_x^{\alpha,\lambda} f(x,t) = e^{-\lambda x} \partial_x^{\alpha}\left[e^{\lambda x} f(x,t)\right] - \lambda^{\alpha} f(x,t) - \alpha \lambda^{\alpha-1} \partial_x f(x,t) \tag{9}$$

where $\alpha \in (1,\ 2]$ (dimensionless) is the fractional index; v $[LT^{-1}]$ and D $[L^{\alpha}T^{-1}]$ are the average velocity and the effective dispersion coefficient, respectively; $\lambda > 0$ $[L^{-1}]$ is the truncation parameter in space; and ω $[ML^{-3}T^{-1}]$ is the mass transfer rate between the two domains. The space fractional derivative in (7) is used here since it was proved to be an efficient tool in capturing super-diffusion with a leading edge or positive skewness for the plume snapshot, due to nonlocal transport along preferential flow paths (Zhang et al., 2015). The truncation parameter λ in model (7) describes the maximum displacement of solute particles due to the finite size of the interconnected, preferential pathways.

The MD-tsFDM (7), which is a simplified distributed-order FDM, assumes dual mobile zones with distinct advective capacities. Model (7) can be conveniently generalized to account for multiple mobile-immobile zones using the distributed-order, spatiotemporal FDM, which however, may not be necessary here. This is because, as discussed in **sections S1** and **S3**, solute transport is dominated by advection in the Monte Carlo models built in this study. It is also noteworthy that the concept of "multiple mobile zones" in model (7) is consistent with that in the mobile-mobile mass exchange model proposed firstly by Ginn (2018) and Lu et al. (2018).

The boundary conditions for the stochastic model (7) are the same as those used for the MT3DMS model discussed in section 2.2. The finite difference method proposed by Baeumer and Meerschaert (2010) is used to solve the MD-tsFDM in this study. To decrease the uncertainty of model parameters, we fix the volumetric proportion of each domain representing the low and large velocity zones, φ_i (i=1, 2), as 0.88 and 0.12, respectively. The porosity of each domain is also assumed to be equal in the MD-tsFDM, following the assumption in Llopis and Capilla (2009) and

Guan et al. (2008). It is noteworthy that the proportion corresponds to the volumetric fraction of lithofacies HGC (=0.12) estimated from the borehole logs. A similar conclusion was drawn by Bianchi and Zheng (2016), who found that the volumetric fraction of HCG corresponds to the calibrated ratio between the mobile and total porosities of the dual-domain transport model. Therefore, in real-world applications, this proportion (φ_i) can be approximated firstly by the volumetric ratio of low- and high-K deposits gleaned from cores, drillers' logs, and/or outcrops.

4.3.1 Bimodal mass distribution

The best-fit results of the mean snapshots for scenario 1 using MD-tsFDMs (7) are shown in **Fig. 9**. The MD-tsFDM (7) with n=2 (two domains) can capture the bimodal plume snapshots better than the single-domain model (n=1). The MD-tsFDM also captures the plume evolution in each domain (shown by the green dashed and dotted line in **Fig. 9**). Compared with the plume in domain 1 (i=1, transport slowly) with a small velocity, the plume in domain 2 (i=2, along the preferential paths) moves faster and dominates the plume front at early time. Additionally, due to the fast advection, the plume moving in the preferential flow path expands quickly in space. Therefore, at late time (i.e., t > 300 days), the 2nd peak (formed by the fast motion) of the plume snapshot tends to be smeared (**Fig. 9**).

Extending upon the previous analysis, we check whether the biomodal (transport or distributiom of the plume) snapshot is due to the initial source size. Previous studies have found that the initial condition of pollutants affects solute transport in heterogeneous media (i.e., Zinn and Harvey, 2003), because different spatial distributions (uniform or flux-weighted) of the initial source can assign different initial velocities to solute particles, thereby impacting subsequent transport behavior (Morales et al., 2017; Puyguiraud et al., 2019). Here we explore another critical, unsolved question of whether a point source can produce bimodal super-diffusion. To explore the impact of initial source conditions on the bimodal transport in alluvial aquifers, we calculate the mass distribution with different initial source lengths at the sampling time of 27 days and 132 days, respectively. Two types of initial source geometry are considered, including a "point" source with a relatively short (2 m) vertical length and a line source with a 40-m vertical length (**Fig. 10**). Results show that the plume for the case with a line source exhibits the bimodal shape at both 27 and 132 days. The plume resulting from the initial point source exhibits a single peak for a relatively short travel distance, which can be fitted by the MD-tsFDM (7) with a single domain. However, when the travel distance increases, even the plume with an initial point source begins to show the significant bimodal snapshot. This result indicates that the velocity field (or the related porous medium architecture setting) is the key factor that controls the bimodal shape of the plume snapshot, while the initial source condition only affects solute transport at early times.

The generally well fit (**Fig. 9**) shows that the MD-tsFDM can capture the bimodal snapshot in alluvial settings with strong heterogeneity (the best-fit results for the other scenarios are shown in **section S6** in the supplementary material) and provides physical intepretation of solute transport in bimodal structure media. The best-fit parameters of the MD-tsFDM (listed in **Table 3**) show the impact of medium architecture on solute transport within each domain. The velocity of the preferential flow path domain (v_2) is much higher than that of the slow domain (v_1), and a larger horizontal mean length leads to a larger v_2. This result is consitent with the analysis in **section 3.2** and **section 4.1**. The dispersivity for transport along the preferential flow domain is much larger than that of the slow domain, (which is expected) and expands quickly the plume 2 **(Fig. 9**). The fractional index, α, of both domains is relatively small (ranging from 1.1 to 1.4), indicating strong heterogeneity for each domain (Benson et al., 2001). The small value of λ demonstrates a long correlation of high-*K* hydrofacies, and generally decreases with an increasing horizontal mean length for hydrofacies (Meerschaert et al., 2008).

4.3.2 Bimodal super-diffusion at the MADE-2 site and the other sites

As discussed above, the MD-tsFDM (7) can successfully capture the bimodal mass distribution in complex alluvial aquifer systems. To check the applicability of model (7) in real-word aquifers, snapshots of the MADE-2 experiment are fitted using the mathematical model (7) proposed herein. The MADE-2 experiment was conducted in the alluvial aquifer located in Columbus, Mississippi, USA, under natural hydraulic gradient conditions. Tracer snapshots were sampled at 27, 132, 224, and 328 days after the injection of 9.7 m^3 tritium solution. For this analysis, we use the last two plume snapshots which were considered to be more reliable and had been thoroughly analyzed in previous studies (Sun et al., 2014; Zhang et al., 2007). Detailed information and review about the MADE-2 experiment can be found in Zheng et al. (2011).

The longitudinal mass distribution for tritium is calculated using the same method described in Bianchi and Zheng (2016). The observed and best-fit mass distributions are plotted in **Fig. 11**. The obvious bimodal pattern of the MADE-2 snapshots provides the field evidence for bi-peak super-diffusion and validates the applicability of the MD-tsFDM (7) to interpret anomalous transport in real-world alluvial aquifer systems on the scale of a few hundred meters.

Multi-peak plume snapshots or tracer BTCs were also observed at the other study sites. For example, Guihéneu et al. (2017) conducted a series of convergent and push-pull tracer experiments and identified various bimodal BTCs. The bimodal snapshots and BTCs were also observed by Hu and Huang (2002) for transport in stochastic heterogeneous dual-permeability media. The MADE-1 tracer test also identified the very similar bimodal snapshots for tracers as those observed for the MADE-2 test (Adams and Gelhar, 1992). The bimodal transport behavior for pollutants was also widely investigated using column or sand-box experiments and numerical experiments (Coppola et al., 2009; Leij and Bradford, 2013; Pedretti et al., 2016; Golfier et al., 2011). The multi-domain models, such as the MD-tsFDM proposed by this study, shed light on the reliable simulation and prediction of pollutant transport in the complex structures mentioned above.

4.4 Impact of hydrofacies HCG on bimodal super-diffusion

It is critical to explore the dominant properties of hydrofacies defined by the transition probability model that generate super-diffusion conditions for solute transport in aquifers. So far, we find that the mean lengths of the hydrofacies affect super-diffusion. In this analysis we explore how other properties of the hydrofacies may impact solute transport and potential super-diffusion observations. Two additional scenarios (scenarios A1 and A2 listed in **Table 4**) were conducted to explore the impact of the volumetric proportion of the coarse grain hydrofacies (i.e., HCG) on super-diffusion. **Fig. 12a** shows the simulated mass distribution at 224 days for different scenarios, in which the global volumetric proportion of HCG increases from 7% to 17%. The proportion of HCG has an obvious impact on super-diffusion by controlling the proportion of the high-velocity zone in the bimodal velocity PDF. A smaller proportion of HCG reduces the size of the high-velocity zone, resulting in a weaker plume front edge and more mass delayed (retained) near the source location. In addition, the simulated mass distribution for the scenario with the lower proportion for HCG (i.e., 7%) also contains more fluctuations of solute mass than the other scenarios (**Fig. 12a**). This result is consistent with the conclusion in Zhang et al. (2013) that found when the proportion of the ancient channel deposits is small (e.g., less than 12%, which is below the percolation threshold (0.14) suggested by Harter (2005) for the 3-*d* model), the high-*K* deposits are not interconnected throughout the entire model domain. Thus, the discontinuous preferential pathways may lead to more local mass peaks in the plume snapshot (**Fig. 12a**).

Second, to further explore the impact of HCG on super-diffusion, we built four additional scenarios (Scenarios A3~A6 listed in **Table 4**) with various horizontal or vertical mean lengths for HCG and the other hydrofacies. The results show that the mean lengths (both thickness and width) of HCG have a prominent impact on bimodal super-diffusion in the alluvial aquifer (**Fig. 12b** and **12c)**. A larger width of HCG (with the other hydrofacies' mean lengths remaining unchanged) enhances the second peak of solute mass, resulting in a heavier (more pronounced) plume front transport (**Fig. 12b**) because of the enhanced connectivity of the most preferential flow pathways. Contrarily, a thicker HCG (while keeping the other hydrofacies's mean lengths unchanged) results in a lighter (less pronounced) plume leading edge (**Fig. 12c**) because of the truncation of the most-permeable transport pathways. This conclusion further expands upon the results provided in Bianchi and Zheng (2016).

Contrarily, the modeled mass distributions are similar for the scenarios where the fine-grain materials were changed to incorporate different mean lengths (thickness or width) while keeping the HCG's mean lengths unchanged, even though the variation of the fine-grained hydrofacies' mean lengths is large (i.e., 1.5 times the hydrofacies' width and 2.5 times the thickness). This result provides a robust explanation as to why none of the thousands of hydrofacies models developed by Zhang et al. (2013) captured the power-law leading edge behavior: there were no extremely high-*K* HCG zones used in their hydrofacies models, which could not produce the 2nd peak in the velocity PDF or the heavy (enhanced) leading plume front of the snapshot.

Overall, these analyses showed that, three primary properties of the hydrofacies HCG impacted super-diffusion. A relatively high *K* distribution, a volumetric proportion of HCG higher than the percolation threshold, and a sufficiently large HCG width for the generated porous medium systems similar to a fracture/matrix system are essential for producing the bimodal super-diffusive snapshots observed at the MADE site. It is noteworthy that, of the three HCG properties, the HCG's mean width contains the highest uncertainty (due to the discontinuous cores/drillers' logs along the longitudinal direction), revealing that additional techniques are needed to reliably define the high-*K* lithofacies' width for such field applications.

5. Conclusion

This study explored the impacts of hydrofacies' mean lengths and the initial source size on bimodal super-diffusion for conservative tracer transport through alluvial aquifers captured by the hydrofacies models built upon the well-known geostatistical tool T-PROGS (Carle and Fogg, 1996, 1997; Carle, 1999). Various scenarios of the hydrofacies models significantly expanded upon the original hydrofacies model for the MADE aquifer developed by Bianchi and Zheng (2016). This expanded analysis was conducted to address the following two questions: (1) there is a historical debate about whether the hydrofacies models for alluvial settings can produce super-diffusion (Zhang et al., 2013); and (2) the detailed impacts of the hydrofacies' thickness/width and the initial source size on super-diffusion remain obscure (Bianchi and Zheng, 2016). By combining Monte Carlo simulations and stochastic model analysis, this study yielded the following five main conclusions, not previously identified, that improve our understanding for the characteristics and description of super-diffusion processes in complex alluvial aquifer settings.

First, Monte Carlo simulations revealed a bimodal velocity distribution with two peaks, which may explain the bimodal distribution of the plume snapshots observed at the MADE site. The bimodal velocity distribution is likely caused by the contrasting K between the hydrofacies HCG and the other hydrofacies at the MADE site (where the K for HCG is two orders of magnitude higher than the other hydrofacies). The 1st peak of the velocity distribution (representing the contribution from the fine grain hydrofacies and not the HCG) captures the relatively low velocity zones that are primarily responsible for delayed transport and the positively skewed plume snapshots. The 2nd peak of the velocity distribution (due to the HCG distribution) accounts for fast motion of solute particles along the preferential flow pathways and the resultant enhanced “heavy” leading plume front observed for the MADE tests. Super-diffusive transport due to the 2nd peak of the velocity distribution can dampen quickly in space and time due to the finite size of the preferential flow paths, making the detection of super-diffusion difficult in real-world aquifers.

Second, the thickness and width of the hydrofacies (especially the high-K HCG) can exhibit different impacts on the spatial pattern of bimodal super-diffusion and associated solute transport. A larger width for the hydrofacies enhances the connectivity of high-permeability deposits (“channels”), resulting in higher values in the bimodal velocity distribution and the enhanced “heavier” plume front. The opposite impact on super-diffusion is identified for the hydrofacies’ mean thickness; i.e., a thicker hydrofacies can retard more solutes near the source and shrink the plume’s leading front.

Third, the size of the initial source affects dynamics of bimodal super-diffusion, due to the fact that the initial source size controls the initial velocity distribution of solute particles. Particularly, a larger initial source results in a more positively skewed plume snapshot, as the particles can experience a wider distribution of velocities (covering both slower and larger velocities). Contrarily, a point source tends to generate a single peak in the plume mass snapshot at early time due to the relatively narrow range of starting velocities and then transitioning to a bimodal pattern in the later plume snapshots after particles sample (experience) greater local velocity variation over time and space..

Fourth, the multi-domain spatial non-local transport model (7), which can be extended from the distributed-order fractional derivative model, can quantify the bimodal super-diffusive transport obtained from the Monte Carlos simulations and the bi-peak tracer snapshots observed at the MADE-2 site. This model may also be applicable for the other aquifers where bi- or multi-peak plumes and/or BTCs were observed. Notably, the slow and fast transport in different domains account for the two peaks of the bimodal velocity distribution, and therefore the stochastic model can capture the negatively skewed plume for pollutants undergoing super-diffusion. The generally well fit shows the applicability of the MD-tsFDM model proposed by this study.

Fifth, as discussed in the supplementary material, additional Monte Carlo simulations and stochastic model analyses are needed to expand the hydrofacies model dimension and capture mixed super- and sub-diffusion processes in alluvial aquifer systems. Our preliminary experiments (shown in the supplementary material) show that the 3-*d* hydrofacies models can enhance the 2nd, fast peak in the bimodal super-diffusion and generate enhanced "heavier" leading plume edges (fronts) than the 2-*d* models, since the lateral extension of the high-*K* hydrofacies enhances the interconnection of high-*K* materials and generates more preferential flow paths for an extended, more pronounced plume front. In addition, the time nonlocal transport components need to be added in the transport model to account for solute retention in complex alluvial aquifers where the Peclet number is small and molecular diffusion controls solute retention. Extensions of both the hydrofacies model and the mobile-mobile model will be discussed in the next study.

Acknowledgments: This work was partially funded by the National Natural Science Foundation of China (grant no. 41931292 and 41722208) and Guangdong Provincial Key Laboratory of Soil and Groundwater Pollution Control (No. 2017B030301012). Results of this study do not reflect the view of the funding agencies.

Reference

Adams, E.E., Gelhar, L.W., 1992. Field study of dispersion in a heterogeneous aquifer: 2. Spatial moments analysis. Water Resour. Res. 28 (12), 3293–3307. https://doi.org/10.1029/92WR01757.

Baeumer, B., Meerschaert, M.M., 2010. Tempered stable Lévy motion and transient super-diffusion. J. Comput. Appl. Math. 233, 2438–2448. https://doi.org/10.1016/j.cam.2009.10.027.

Benson, D.A., Schumer, R., Meerschaert, M.M., Wheatcraft, S.W., 2001. Fractional Dispersion, Lévy Motion, and the MADE Tracer Tests. Transp. Porous Med. 42, 211–240. https://doi.org/10.1023/A:1006733002131.

Berkowitz, B., Cortis, A., Dentz, M., Scher, H., 2006. Modeling non-Fickian transport in geological formations as a continuous time random walk. Rev. Geophys. 44, RG2003. https://doi.org/10.1029/2005RG000178.

Bianchi, M., Zheng, M.C., 2016. A lithofacies approach for modeling non-Fickian solute transport in a heterogeneous alluvial aquifer. Water Resour. Res. 52 (1), 552–565. https://doi.org/10.1002/2015WR018186.

Bianchi, M., Pedretti, D., 2017. Geological entropy and solute transport in heterogeneous porous media. Water Resour. Res. 53, 4691-4708. https:// doi.org/10.1002/2016WR020195.

Bianchi, M., Pedretti, D., 2018. An entrogram-based approach to describe spatial heterogeneity with applications to solute transport in porous media. Water Resour. Res. 54, 4432-4448. https://doi.org/10.1029/2018WR022827.

Boggs, J.M., Young, S.C., Benton, D.J., Chung, Y.C., 1990. Hydrogeologic characterization of the MADE site, Tech. Rep. EN-6915, Electr. Power. Res. Inst, Palo Alto, Calif.

Bouchaud, J.P., Georges, A., 1990. Anomalous diffusion in disordered media: Statistical mechanisms, models and physical applications. Phys. Rep. 195, 127–293. https://doi.org/10.1016/0370-1573 (90)90099-N.

Carle, S.F., 1999. T-PROGS: Transition Probability Geostatistical Software. Version 2.1., University of California, Davis.

Carle, S.F., Fogg, G.E., 1996. Transition probability-based indicator geostatistics. Math. Geol. 28, 453–476. https://doi.org/10.1007/bf02083656.

Carle, S.F., Fogg, G.E., 1997. Modeling Spatial Variability with One and Multidimensional Continuous-Lag Markov Chains. Math. Geol. 29, 891–918. https://doi.org/10.1023/A:1022303706942.

Chechkin, A.V., Gorenflo, R., Sokolov, I.M., 2002. Retarding subdiffusion and accelerating superdiffusion governed by distrinuted-order fractional diffusion equations. Phys. Rev. E 66, 046129. https://doi.org/ 10.1103/PhysRevE.66.04612.

Coppola, A., Comegna, V., Basile, A., Lamaddalena, N., Severino, G., 2009. Darcian preferential water flow and solute transport through bimodal porous systems: Experiments and modelling. J. Contam. Hydrol. 104, 74–83. https://doi.org/10.1016/j.jconhyd.2008.10.004.

Dentz, M., Le Borgne, T., Lester, D.R., De Barros, F.P.J., 2015. Scaling forms of particle densities for Lévy walks and strong anomalous diffusion. Phys. Rev. E - Stat. Nonlinear Soft Matter Phys. 92, 032128. https://doi.org/10.1103/PhysRevE.92.032128.

Dentz, M., Bolster, D., 2010. Distribution-versus correlation-induced anomalous transport in quenched random velocity fields. Phys. Rev. Lett. 105, 244301. https://doi.org/10.1103/PhysRevLett.105.244301.

Diethelm, K., Ford, N.J., 2009. Numerical analysis for distributed-order differential equations. J. Comput. Appl. Math. 225(1), 96-104. https://doi.org/10.1016/j.cam.2008.07.018.

Eab, C.H., Lim, S.C., 2011. Fractional Langevin equations of distributed order. Phys. Rev. E, 83, 031136. https://doi.org/ 10.1103/PhysRevE.83.031136.

Fogg, G.E., Zhang, Y., 2016. Debates-Stochastic subsurface hydrology from theory to practice: A geologic perspective. Water Resour. Res. 52 (12), 9235–9245. https://doi.org/10.1002/2016WR019699.

Ginn, T. R., 2018. Modeling bimolecular reactive transport with mixing-limitation: Theory and application to column experiments. Water Resour. Res. 54 (1), 256–270. https://doi.org/10.1002/ 2017WR022120.

Gorenflo, R., Luchko, Y., Yamamoto, M., 2015. Time-fractional diffusion equation in the fractional sobolev spaces. Fract. Calc. Appl. Anal. 18 (3), 799–820. https://doi.org/10.1515/fca-2015-0048.

Golfier, F., Quintard, M., Wood, B.D., 2011. Comparison of theory and experiment for solute transport in weakly heterogeneous porous medium. Adv. Water Resour. 34, 899–914. https://doi.org/ 10.1016/j.advwatres.2011.04.019.

Guan, J., Molz, F.J., Zhou, Q., Liu, H.H., Zheng, C., 2008. Behavior of the mass transfer coefficient during the MADE-2 experiment: New insights. Water Resour. Res. 44 (2), W02423. https://doi.org/10.1029/2007WR006120.

Guihéneuf, N., Bour, O., Boisson, A., Borgne, T. Le, Becker, M.W., Nigon, B., Wajiduddin, M., Ahmed, S., Maréchal, J., 2017. Insights about transport mechanisms and fracture flow channeling from multi-scale observations of tracer dispersion in shallow fractured crystalline rock. J. Contam. Hydrol. 206, 18–33. http://dx.doi.org/10.1016/j.jconhyd.2017.09.003.

Haggerty, R., Gorelick, S.M., 1995. Multiple-rate mass transfer for modeling diffusion and surface reactions in media with pore-scale heterogeneity. Water Resour. Res. 31, 2383–2400. https://doi.org/10.1029/95WR10583.

Harbaugh, A.W., 2006. MODFLOW-2005, The U.S. Geological Survey Modular Ground-water Model—The Ground-water Flow Process, U.S. Geol. Tech. Methods, 6-A16.

Harter, T., 2005. Finite-size scaling analysis of percolation in three-dimensional correlated binary Markov chain random fields. Phys. Rev. E - Stat. Nonlinear Soft Matter Phys. 72, 1–8. https://doi.org/10.1103/PhysRevE.72.026120.

Herrick, M.G., Benson, D.A., Meerschaert, M.M., McCall, K.R., 2002. Hydraulic conductivity, velocity, and the order of the fractional dispersion derivative in a highly heterogeneous system. Water Resour. Res. 38 (11), 1227. https://doi.org/10.1029/2001wr000914.

Hu, B.X., Huang, H., Zhang, D., 2002. Stochastic analysis of solute transport in heterogeneous, dual-permeability media. Water Resour. Res. 38 (9), 1175. https://doi.org/10.1029/2001wr000442.

Hyman, J.D., Dentz, M., Hagberg, A., Kang, P.K., 2019. Linking structural and transport properties in three-dimensional fracture network. J. Geophys. Res. Solid Earth 124, 1185-1204. https://doi.org/10.1029/2018JB016553.

Kohlbecker, M. V., Wheatcraft, S.W., Meerschaert, M.M., 2006. Heavy-tailed log hydraulic conductivity distributions imply heavy-tailed log velocity distributions. Water Resour. Res. 42 (4), W04411. https://doi.org/10.1029/2004WR003815.

Leij, F.J., Bradford, S.A., 2013. Colloid transport in dual-permeability media. J. Contam. Hydrol. 150, 65–76. https://doi.org/10.1016/j.jconhyd.2013.03.010.

Llopis-Albert, C., Capilla, J.E., 2009. Gradual conditioning of non-Gaussian transmissivity fields to flow and mass transport data: 3. Application to the Macrodispersion Experiment (MADE-

2) site, on Columbus Air Force Base in Mississippi (USA). J. Hydrol. 371, 75–84. https://doi.org/10.1016/j.jhydrol.2009.03.016.

Lorenzo, C.F., Hartley, T.T., 2002. Variable order and distributed order fractional operators. Nonlinear Dyn. 29, 57-98.

Lu, C.H., Wang, Z., Zhao, Y., Rathore, S.S., Huo, J., Tang, Y., Lu, M., Gong, R., Cirpka, O.A., Luo, J., 2018. A mobile-mobile transport model for simulating reactive transport in connected heterogeneous fields. J. Hydrol. 560, 97–108. https://doi.org/10.1016/j.jhydrol.2018.02.073.

Mainardi, F., Mura, A., Pagnini, G., Gorenflo, R., 2008. Time-fractional diffusion of distributed order. J. Vib. Control 14, 1267–1290. https://doi.org/ 10.1177/1077546307087452.

Meerschaert, M.M., Zhang, Y., Baeumer, B., 2008. Tempered anomalous diffusion in heterogeneous systems. Geophys. Res. Lett. 35, L17403. https://doi.org/10.1029/2008GL034899.

Miller, K.S., Ross, B., 1993. An Introduction to Fractional Calculus and Fractional Differential Equations. John Wiley, Hoboken, N. J.

Morales, V.L., Dentz, M., Willmann, M., Holzner, M., 2017. Stochastic dynamics of intermittent pore-scale particle motion in three-dimensional porous media: Experiments and theory. Geophys. Res. Lett. 44, 9361–9371. https://doi.org/10.1002/2017GL074326.

Pedretti, D., Molinari, A., Fallico, C., Guzzi, S., 2016. Implications of the change in confinement status of a heterogeneous aquifer for scale-dependent dispersion and mass-transfer processes. J. Contam. Hydrol. 193, 86–95. https://doi.org/10.1016/j.jconhyd.2016.09.005.

Puyguiraud, A., Gouze, P., Dentz, M., 2019. Stochastic Dynamics of Lagrangian Pore-Scale Velocities in Three-Dimensional Porous Media. Water Resour. Res. 55 (2), 1196–1217. https://doi.org/10.1029/2018WR023702.

Saadatfar, M., Sahimi, M., 2002. Diffusion in disordered media with long-range correlations: Anomalous, Fickian, and superdiffusive transport and log-periodic oscillations. Phys. Rev. E - Stat. Physics Plasmas Fluids Relat. Interdiscip. Top. 65, 1–8. https://doi.org/10.1103/PhysRevE.65.036116.

Sahimi, M., 1993. Flow phenomena in rocks: from continuum models to fractals, percolation, cellular automata, and simulated annealing. Rev. Mod. Phys. 65, 1393–1534. https://doi.org/10.1103/RevModPhys.65.1393.

Salamon, P., Fernàndez-Garcia, D., Gómez-Hernández, J.J., 2007. Modeling tracer transport at the MADE site: The importance of heterogeneity. Water Resour. Res. 43 (8), W08404. https://doi.org/10.1029/2006WR005522.

Schumer, R., Benson, D. A., Meerschaert, M.M., Baeumer, B., 2003a. Fractal mobile/immobile solute transport. Water Resour. Res. 39 (10), 1296. https://doi.org/10.1029/2003WR002141.

Schumer, R., Benson, D.A., Meerschaert, M.M., Baeumer, B., 2003b. Multiscaling fractional advection-dispersion equations and their solutions. Water Resour. Res. 39 (1), 1022. https://doi.org/10.1029/2001WR001229.

Sun, H., Zhang, Y., Chen, W., Reeves, D.M., 2014. Use of a variable-index fractional-derivative model to capture transient dispersion in heterogeneous media. J. Contam. Hydrol. 157, 47–58. https://doi.org/10.1016/j.jconhyd.2013.11.002

Tyukhova, A., Dentz, M., Kinzelbach, W., Willmann, M., 2016. Mechanisms of anomalous dispersion in flow through heterogeneous porous media. Phys. Rev. Fluids 1, 074002. https://doi.org/10.1103/PhysRevFluids.1.074002.

Veneziano, D., Essiam, E., 2004. Nonlinear spectral analysis of flow through multifractal porous media. Chaos Solitons Fractals, 19, 293-307. https://doi.org/10.1016/S0960-0779(03)00043-2.

Veneziano, D., Tabaei, A., 2004. Nonlinear spectral analysis of flow through porous media with isotropic lognormal hydraulic conductivity. J. Hydrol. 294, 4-17. https://doi.org/10.1016/j.jhydrol.2003.10.025.

Zhang, Y., Benson, D.A., Meerschaert, M.M., LaBolle, E.M., 2007. Space-fractional advection-dispersion equations with variable parameters: Diverse formulas, numerical solutions, and application to the Macrodispersion Experiment site data. Water Resour. Res. 43 (5), W05439. https://doi.org/10.1029/2006WR004912.

Zhang, Y., LaBolle, E.M., Pohlmann, K., 2009. Monte Carlo simulation of superdiffusion and subdiffusion in macroscopically heterogeneous media. Water Resour. Res. 45 (10), W10417. https://doi.org/10.1029/2008WR007448.

Zhang, Y., Baeumer, B., Reeves, D.M., 2010. A tempered multiscaling stable model to simulate transport in regional-scale fractured media. Geophys. Res. Lett. 37 (11), L11405. https://doi.org/10.1029/2010GL043609.

Zhang, Y., Green, C.T., Fogg, G.E., 2013. The impact of medium architecture of alluvial settings on non-Fickian transport. Adv. Water Resour. 54, 78–99. https://doi.org/10.1016/j.advwatres.2013.01.004.

Zhang, Y., Meerschaert, M.M., Baeumer, B., LaBolle, E.M., 2015. Modeling mixed retention and early arrivals in multidimensional heterogeneous media using an explicit Lagrangian scheme. Water Resour. Res. 51 (8), 6311–6337. https://doi.org/10.1002/2015WR016902.

Zheng, C., Bianchi, M., Gorelick, S.M., 2011. Lessons learned from 25 years of research at the MADE site. Ground Water 49, 649–662. https://doi.org/10.1111/j.1745-6584.2010.00753.x.

Zheng, C., 2010. MT3DMS v5.3: Supplemental User's Guide. Tech. Rep. 51. https://doi.org/10.1038/s41559-017-0279-3.

Zinn, B., Harvey, C.F., 2003. When good statistical models of aquifer heterogeneity go bad: A comparison of flow, dispersion, and mass transfer in connected and multivariate Gaussian hydraulic conductivity fields. Water Resour. Res. 39 (3), 1051. https://doi.org/10.1029/2001WR001146.

Table 1. Geostatistics and hydraulic properties of each of the five hydrofacies. In the legend, "*K*" denotes the hydraulic conductivity, "HCG" represents Highly Conductive Gravel, "GS" represents gravel with sand, "SGF" represents Sand Gravel and Fines, "SG" represents Sand and Gravel, "S" represents well-sorted Sand, and "*Pe*" denotes the Peclet number.

Hydrofacies	Width (m)	Thickness [m]	Proportion [-]	Porosity [-]	*K* [m/d]	*Pe* [-]
SGF	39	0.9	0.35	0.259	2.52	1.68×10^{4}
S	35	1.7	0.21	0.415	5.65	5.64×10^{4}
HCG	30	1	0.12	0.265	303.39	4.54×10^{6}
SG	25	0.4	0.14	0.298	7.74	8.27×10^{4}
GS	31	0.5	0.18	0.257	6.76	6.97×10^{4}

Table 2. Characteristic parameters of the velocity PDF. In the legend, v_{p1} and v_{p2} denote the peak of the low and high velocity zones, respectively; v_m is the velocity with the lowest probability distributed between v_{p1} and v_{p2}; and $\mathrm{P}(\mathrm{v} \leq v_m)$ denotes the percentage of the low velocity zone. The units for velocity are m/d.

Mean Length	Scenario 1 (1.0Z)	Scenario 2 (1.5Z)	Scenario 3 (2.0Z)	Scenario 4 (2.5Z)	Scenario 5 (1.25X)	Scenario 6 (1.5X)	Scenario 7 (2.0X)
v_{p1}	0.32	0.32	0.37	0.37	0.32	0.24	0.28
v_{p2}	3.89	3.39	1.95	1.95	4.47	5.89	6.76
v_m	1.70	1.70	1.70	1.70	1.94	1.94	2.24
$\mathrm{P}(\mathrm{v} \leq v_m)$	0.91	0.92	0.94	0.92	0.90	0.90	0.89

Table 3. The best-fit parameters of the MD-tsFDM (7) for all scenarios. The superscript "*" denotes the hydrofacies simulated conditionally, and "SL" means the vertical source length.

Scenario	Mean length	v_1 [m/d]	v_2 [m/d]	D_1 [m^2/d]	D_2 [m^2/d]	α_1 [-]	α_2 [-]	λ_1 [m^{-1}]	λ_2 [m^{-1}]	ω [$mgL^{-1}d^{-1}$]
1	1.0X 1.0Z	0.15	0.6	0.5	1.9	1.3	1.25	0.005	0.03	0.0005
2	1.5Z	0.13	0.6	0.45	2.1	1.3	1.3	0.007	0.025	0.0006
3	2.0Z	0.11	0.55	0.5	1.2	1.1	1.3	0.01	0.03	0.0004
4	2.5Z	0.11	0.5	0.55	1.4	1.1	1.3	0.02	0.025	0.0007
5	1.25X	0.15	0.85	0.5	1.9	1.3	1.3	0.008	0.02	0.0007
6	1.5X	0.25	0.9	0.6	2.1	1.1	1.4	0.0001	0.015	0.0008
7	2.0X	0.17	1.45	0.55	1.8	1.1	1.4	0.003	0.00001	0.0012
8* (SL=40m)	1.0X 1.0Z	0.1	0.8	0.3	2.4	1.25	1.15	0.01	0.03	0.001
8* (SL=2m) 27 days	1.0X 1.0Z	-	1.05	-	2.7	-	1.5	-	0.02	-
8* (SL=2m) 132 days	1.0X 1.0Z	0.45	1.25	1.25	1.9	1.25	1.25	0.015	0.06	0.0006

Table 4. Additional scenarios built in **section 4.4** to explore the impact of HCG properties on bimodal super-diffusion.

Scenario	HCG Thickness	HCG Width	HCG proportion	Other hydrofacies thickness	Other hydrofacies width
A1	1.0Z	1.0X	7%	1.0Z	1.0X
A2	1.0Z	1.0X	17%	1.0Z	1.0X
A3	1.0Z	1.5X	12%	1.0Z	1.0X
A4	1.0Z	1.0X	12%	1.0Z	1.5X
A5	2.5Z	1.0X	12%	1.0Z	1.0X
A6	1.0Z	1.0X	12%	2.5Z	1.0X

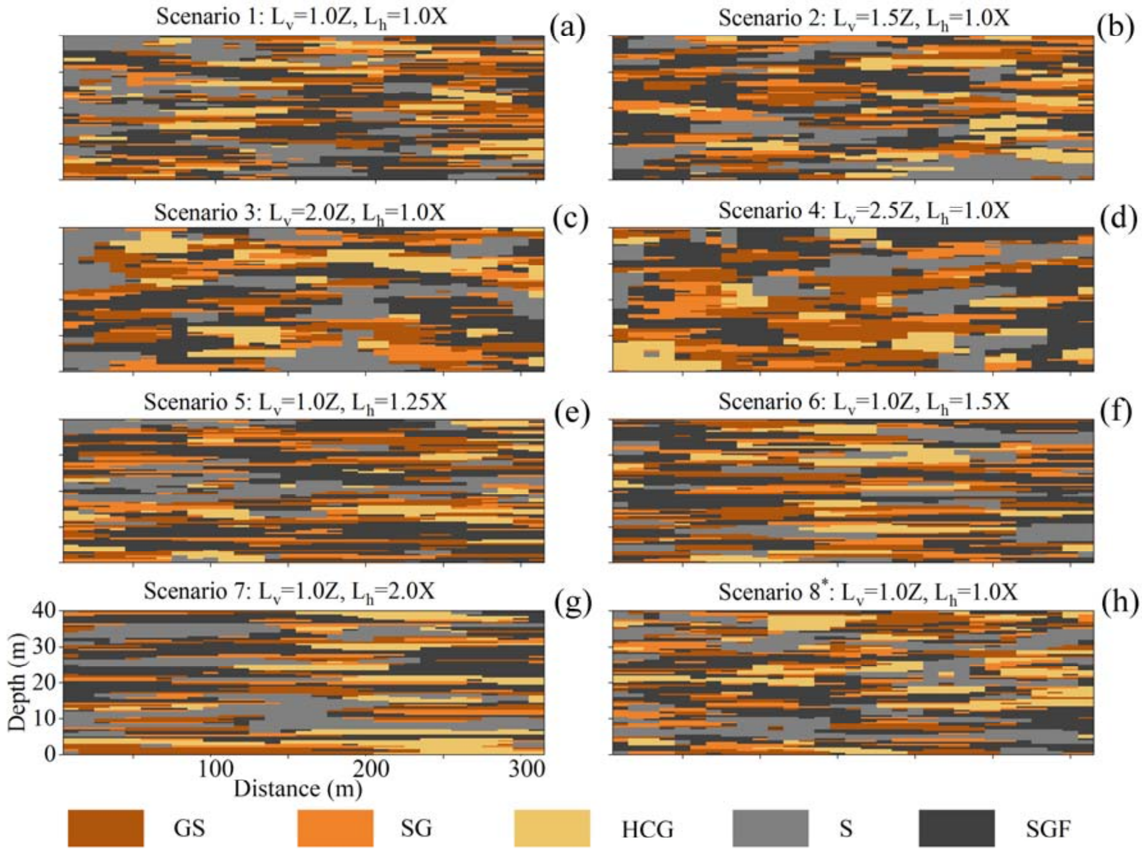

Fig. 1. One realization of the hydrofacies model for each scenario (8 scenarios total). L_v and L_h are mean length of hydrofacies in vertical and horizontal direction, Z and X denote the mean thickness and longitudinal mean length for the hydrofacies for the base case (which is Scenario 1), respectively.

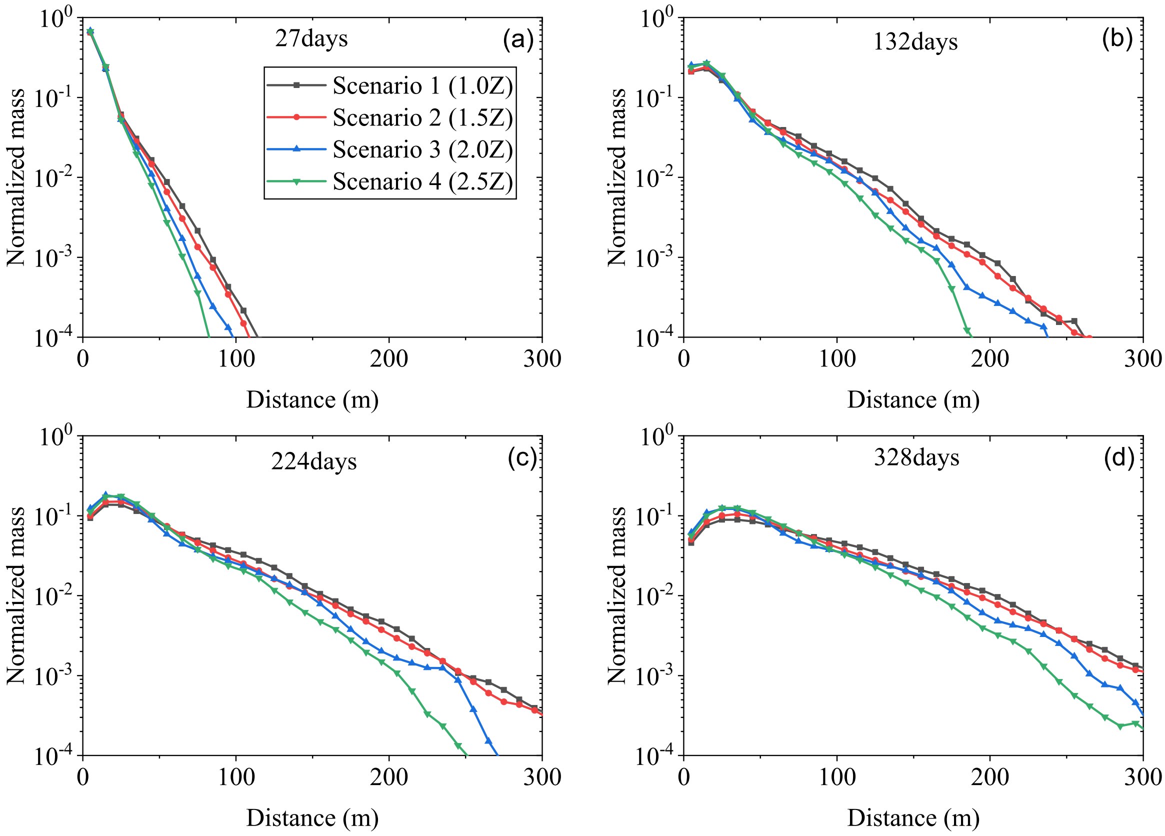

Fig. 2. The simulated normalized mass distribution at 27 days (a), 132 days (b), 224 days (c), and 328 days (d) after the instantaneous source was released, for four scenarios of hydrofacies models with different vertical mean lengths. In the legend, "1.0Z, 1.5Z, 2.0Z, and 2.5Z" denote that the vertical mean length is 1.0, 1.5, 2.0, and 2.5 times of the base case, respectively.

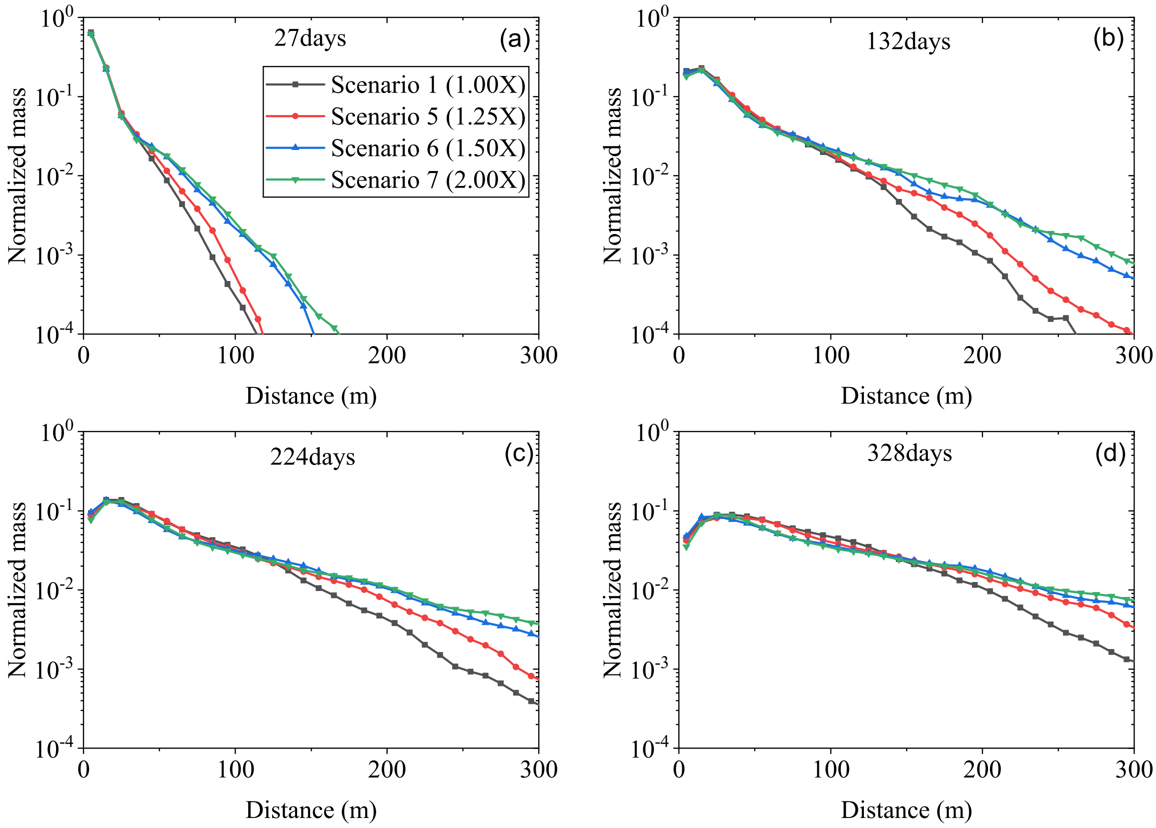

Fig. 3. The simulated evolution of (normalized) plume snapshots at 27 days (a), 132 days (b), 224 days (c), and 328 days (d) after the release of an instantaneous source for scenarios of hydrofacies models with different longitudinal mean lengths. The legend "X" denotes the longitudinal mean length, and the number "1.0, 1.5, 2.0 and 2.5" denotes the ratio of the longitudinal mean length between the scenario and the base case.

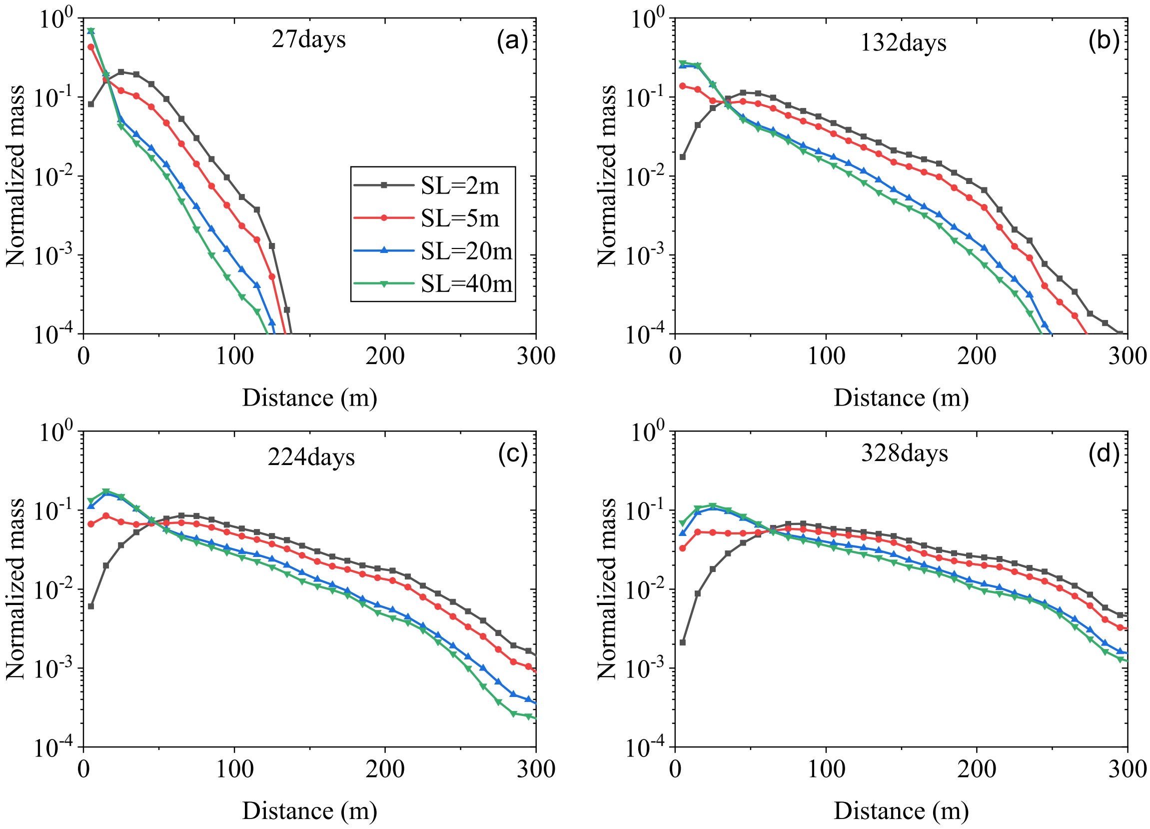

Fig. 4. The simulated and normalized mass distribution for contaminants at 27 days (a), 132 days (b), 224 days (c), and 328 days (d) after the source release for scenarios with various sizes of the initial line source (scenarios 8). The legend "SL=2m" means that the source length is 2 m.

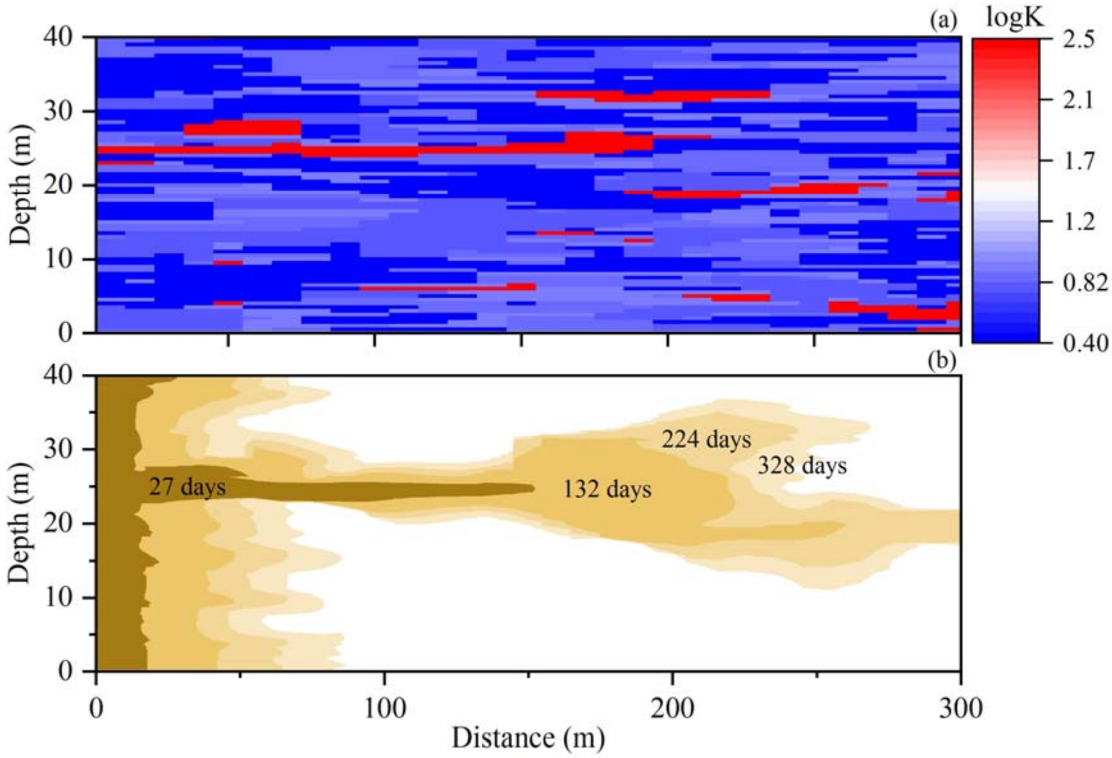

Fig. 5. The simulated spatial distribution of $\log_{10}(K)$ field (a) and the temporal evolution of the simulated plume front ($C = 0.01C_0$) (b), for one realization of Scenario 1.

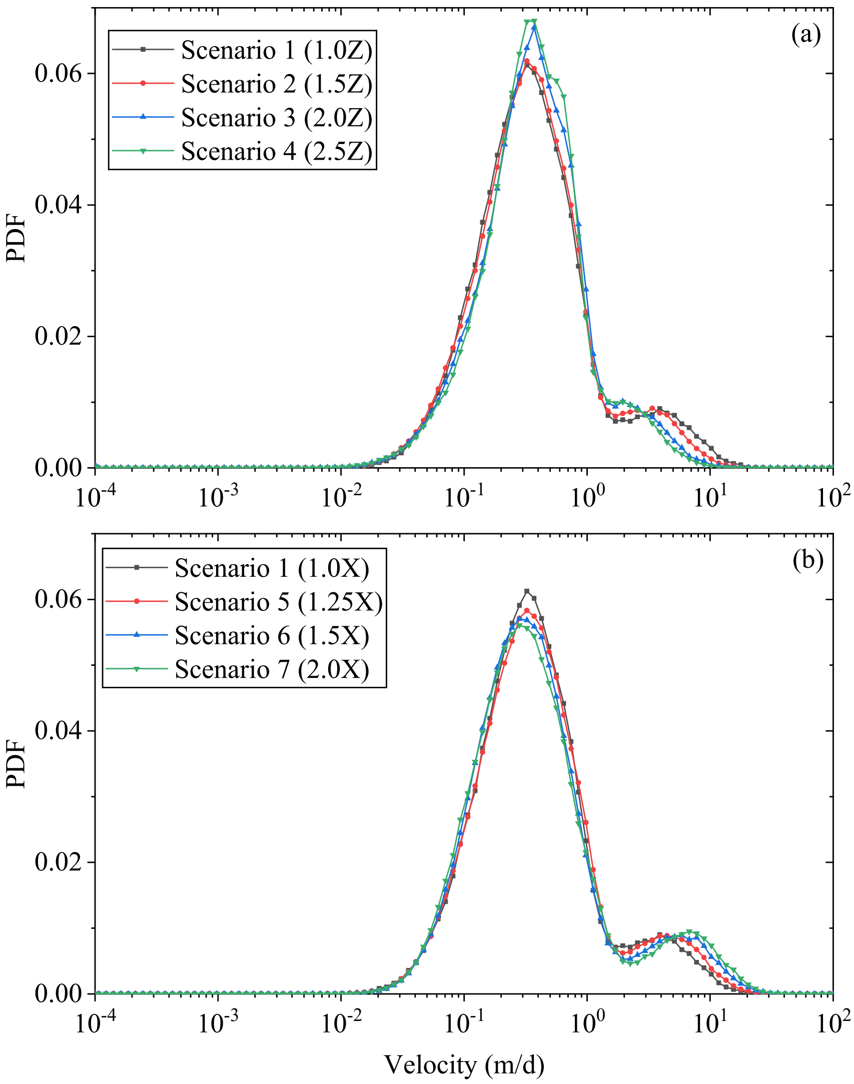

767

768 **Fig. 6.** The PDF of the velocity for scenarios with different thicknesses (a) and different widths (b).

769

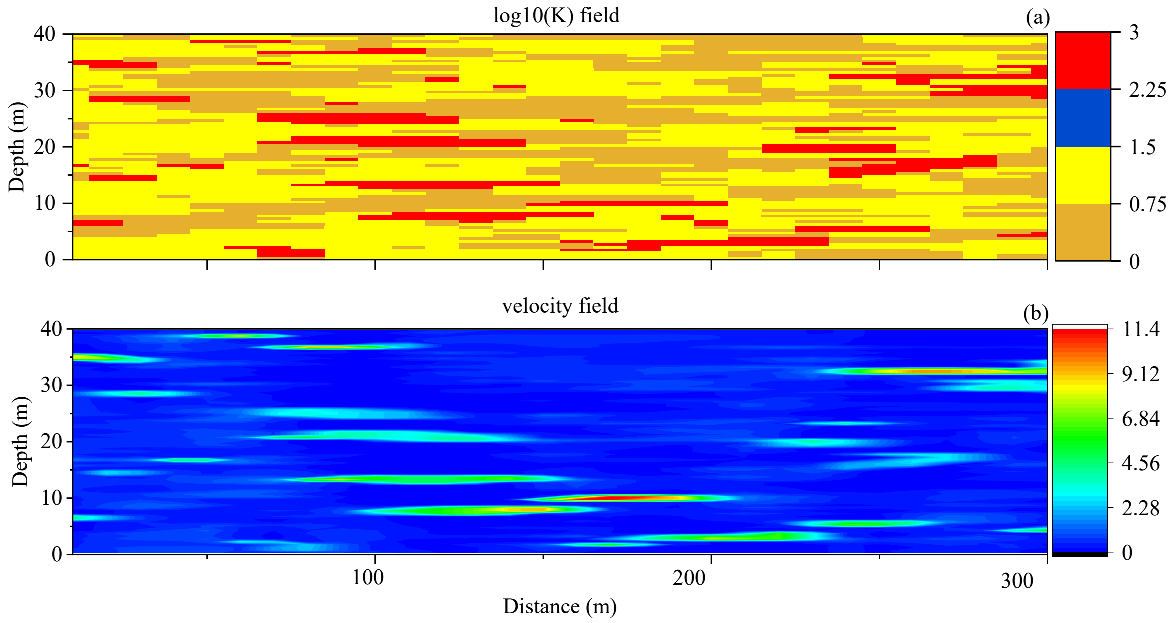

Fig. 7. One realization of the simulated spatial distribution of hydraulic conductivity and the longitudinal velocity for scenario 1: the $\log_{10}(K)$ field (m/d) (a) and the corresponding spatial distribution of velocity (m/d) (b).

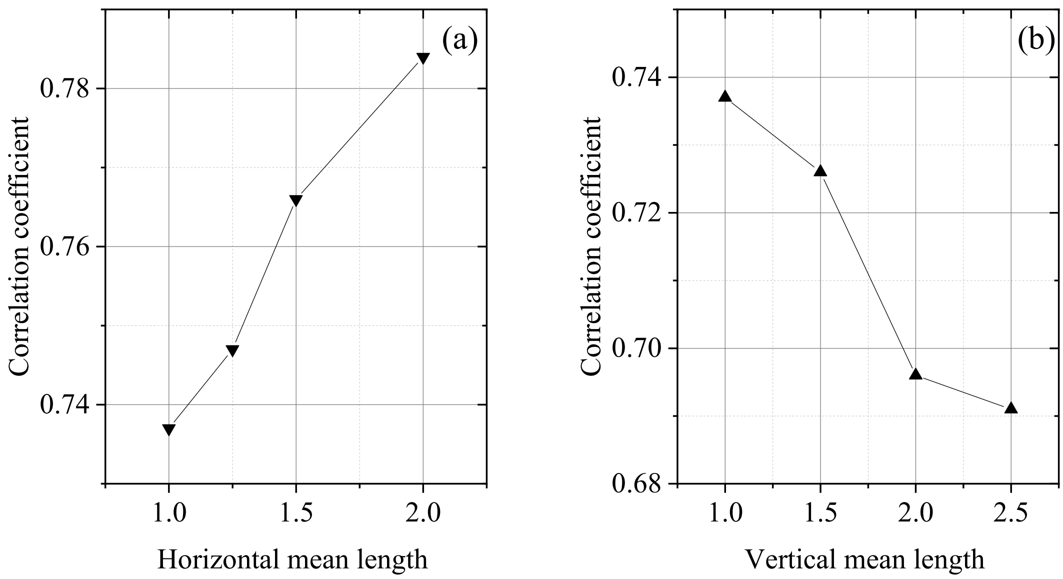

Fig. 8. The correlation coefficient between the spatial distribution of hydraulic conductivity and the longitudinal velocity for scenarios with different longitudinal mean lengths (Scenarios 1, 5, 6, and 7) (a) and mean thicknesses (Scenarios 1, 2, 3, and 4) (b).

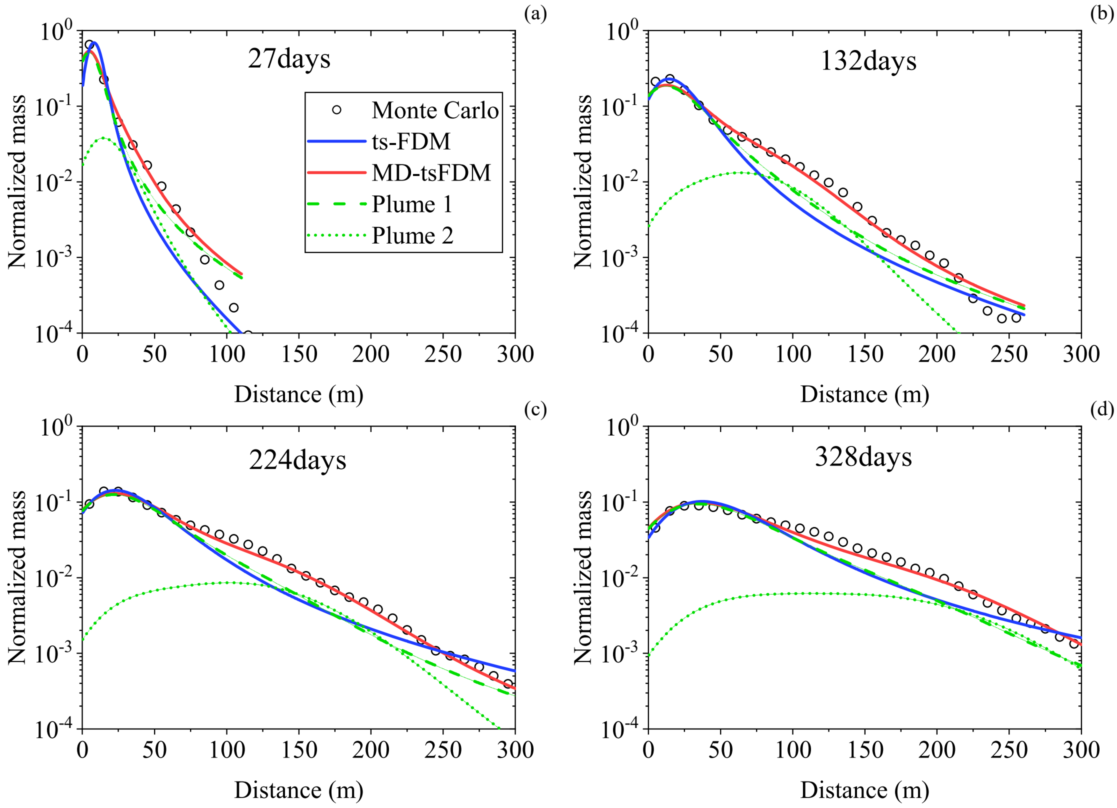

Fig. 9. The Monte Carlo results for scenario 1 (symbols) versus the best-fit snapshots for the tempered space fractional-derivative model with a single domain (the blue line, e.g., tsFDM) or two domains (the red line, e.g., MD-tsFDM) at 27 days (a), 132 days (b), 224 days (c), and 328 days (d) after the source release. Plume 1 (green dash line) and plume 2 (green dot line) denote the plume of MD-tsFDM within domain 1 and domain 2, respectively.

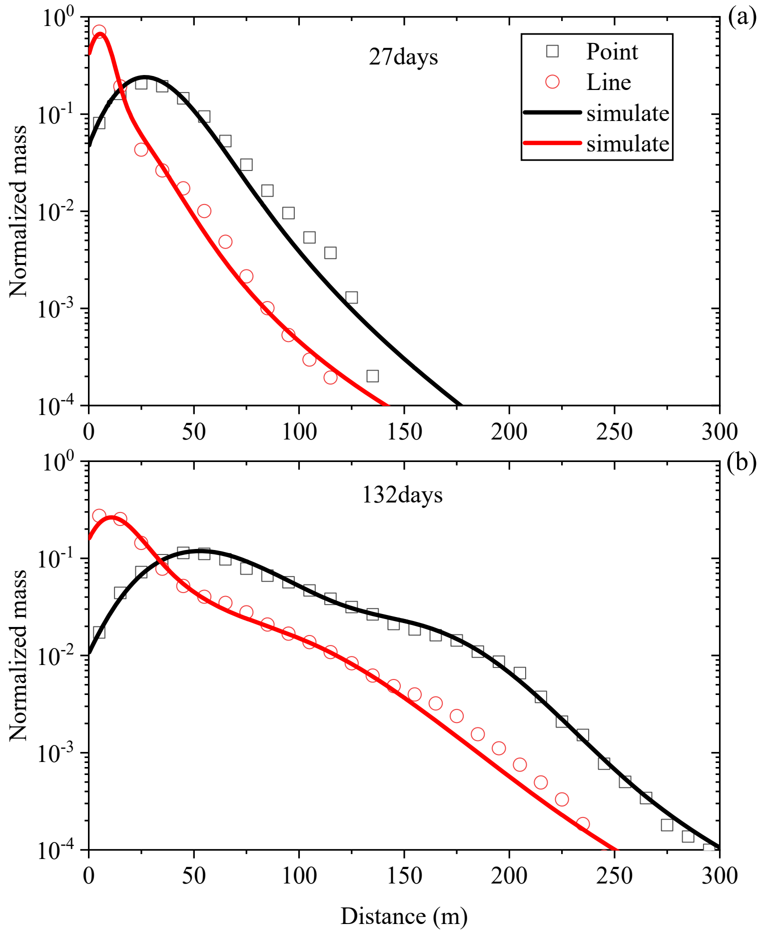

Fig. 10. The Monte Carlo results (symbols) versus the best-fit solutions (lines) using the MD-tsFDM for the plume snapshot at 27 days (a) and 132 days (b), respectively, after releasing an instantaneous point source (the black rectangles) or a line source (the red dots) for Scenario 8.

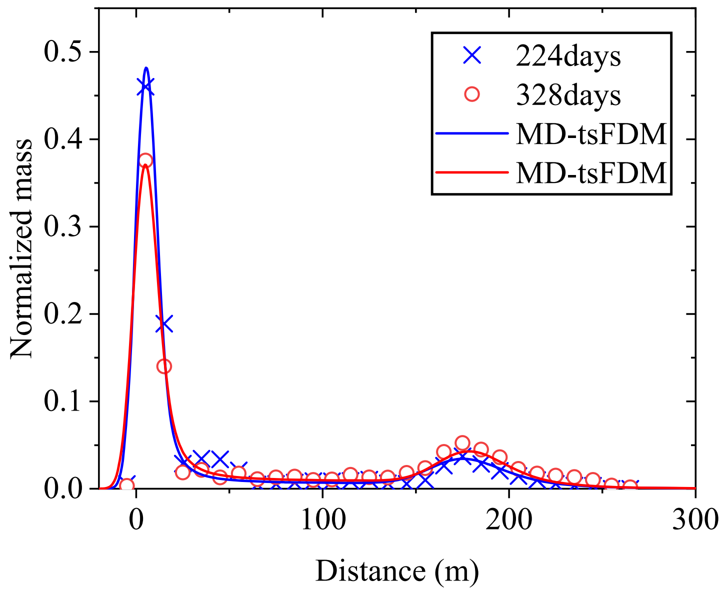

Fig. 11. The longitudinal mass distribution of tritium observed in the MADE-2 experiment (symbols) and the best-fit results (lines) using the MD-tsFDM (7) at the sampling cycle 224 days (blue) and 328 days (red), respectively.

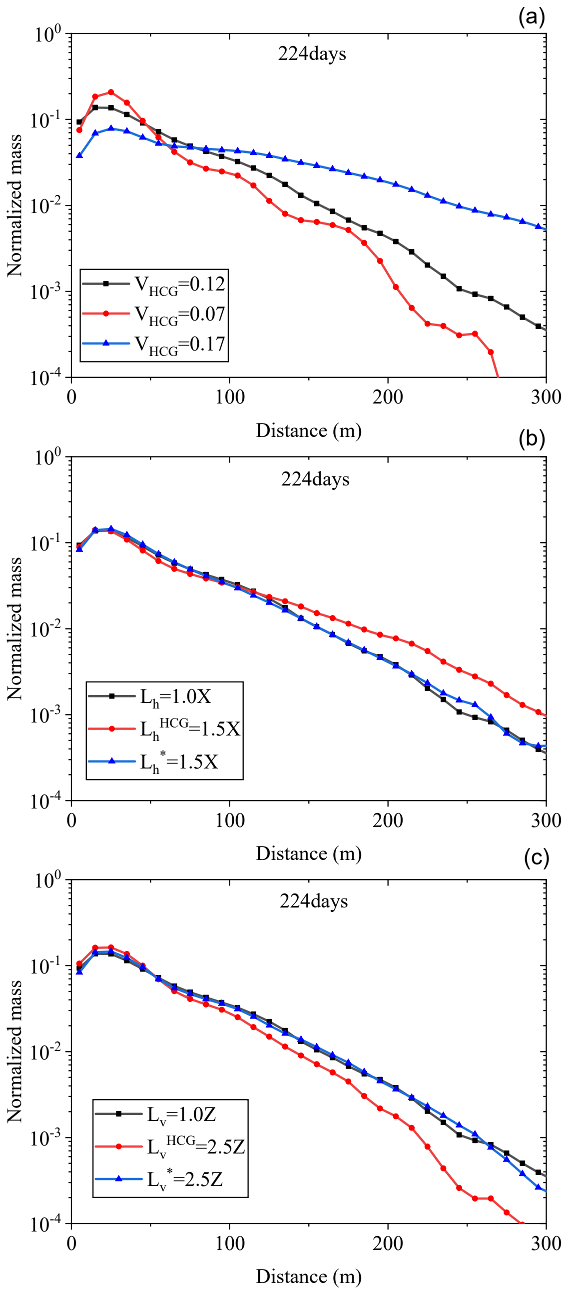

Fig. 12. Major factors controlling super-diffusion, including the volumetric proportion of HCG (a), the horizontal mean length of HCG (denoted by L_h^{HCG}) and the other hydrofacies (denoted by L_h^{*}) (b), the vertical mean length of HCG (denoted by L_v^{HCG}) and the other hydrofacies (denoted by L_v^{*}) (c).